Local Structure of the Proton Conducting System $Ba_2In_{1.85}M_{0.15}O_5$ (M = Ga, Sc, In, Y) Investigated with Infrared Spectroscopy

DHARSHANI EKANAYAKE

CHALMERS

Department of Applied Physics
CHALMERS UNIVERSITY OF TECHNOLOGY
Göteborg, Sweden 2013

Local structure of the proton conducting brownmillerite system $Ba_2In_{1.85}M_{0.15}O_5$ (M = Ga, Sc, In, Y) investigated with infrared spectroscopy

DHARSHANI EKANAYAKE

© DHARSHANI EKANAYAKE, 2013.

Department of Applied Physics

Chalmers University of Technology

SE-412 96 Gothenburg

Sweden

Telephone + 46 (0)31-772 1000

Chalmers Reproservice

Göteborg, Sweden 2013

Abstract

This thesis concerns experimental studies on the proton conducting brownmillerite type oxide system, $Ba_2In_{1.85}M_{0.15}O_5$ (M = Ga, Sc, In, Y), of interest as potential proton conducting electrolytes for next-generation fuel cells operating in the temperature range from ~200 to ~500 °C. This temperature range is more suitable for practical applications but today's available electrolytes do not show satisfactory performance. To develop new materials as electrolytes with better performances a deeper understanding of the structure and the proton dynamics of the material is required.

Protons in the $Ba_2In_{1.85}M_{0.15}O_5$ (M= Ga, Sc, In, Y) system have been introduced by hydration. How the dopant atoms influence the structure and proton dynamics of the material is the key issue to understand. Using infrared spectroscopy, such properties have here been investigated.

The results show that the material structure becomes distorted with incorporation of dopant atoms. Also the results show that the symmetry of material's structure increases upon hydration. Furthermore, the results indicate that smaller atomic radius of the dopant results in a higher tendency of hydrogen bond formation between the protons and neighboring oxygens.

Keywords: brownmillerite type oxides, proton conduction, hydrogen bonding, infrared spectroscopy.

Table of Contents

1. Introduction 1

2. Proton conducting brownmillerite type oxides 5

2.1 The brownmillerite structure and incorporation of protons 6

2.2 Proton conductivity of brownmillerites 7

3. Infrared spectroscopy 9

3.1 The measurement principle 9

3.2 Measurements.. 10

3.3 Instrumentation 11

3.3.1 The Bruker Alpha FT-IR spectrometer 11

3.3.2 The Bruker IFS66 spectrometer 11

4. Results and discussion 13

4.1 Results in the frequency range 40-1000 cm^{-1} 13

4.2 Results in the frequency range 1750-4000 cm^{-1} 14

5. Conclusions 19

A Fuel cells 21

Acknowledgements 25

Bibliography 27

CHAPTER 1

Introduction

The development of alternative, cleaner, power devices is one of the major worldwide challenges, since we have to deal with the limitation of fossil fuel reserves, increasing energy demand as well as the global warming which is a major environmental threat. Developing energy conversion and storage technologies, which produce minimum or no polluting emissions, would be a practical solution for this. The performance of these technologies depends on the properties of their component materials, however because of difficulties in finding sufficiently good component materials the development of most alternative energy technologies has stagnated. Therefore, the development of new materials, with improved performance, is a major requirement for further advancement.

A particularly promising, yet challenging, alternative energy technology is the fuel cell. This is an electrochemical device, which converts chemical energy into electrical energy in an environmentally friendly way. At the heart of these devices is an oxide-ion or proton conducting electrolyte, which transports ions from one side of the cell to the other. In a simple picture, the transportation of ions occurs in one of the following two ways, (i) by the Grotthuss or (ii) by the vehicular mechanism. In the Grotthuss mechanism, the proton transfers from one site to another, often via the creation of a transfer-assisting hydrogen bond between the proton and the atom it will jump to, whereas in the vehicle mechanism the proton diffuses together with an ion or molecule (e.g. H_3O^+) that acts as a vehicle. The vehicle mechanism is frequently encountered in aqueous solutions and other liquids/melts, whereas the Grotthuss mechanism is often present in solids. High proton conductivity, long-term stability, low cost and being electronically insulating are the main properties of an ideal electrolyte.

Today, fuel cells work either at high temperatures (500-1000 °C) [solid oxide fuel cells (SOFCs)] or at low temperatures (<200 °C) [polymer electrolyte membrane fuel cells (PEMFCs)]. However, fuel cells operating in these temperature ranges,

all have some crucial disadvantages related to them. For example, PEMFCs need a noble-metal catalyst (typically platinum) to be used to separate electrons and protons of the hydrogens, which increase the cost of the cell. In addition, platinum is extremely sensitive to carbon monoxide (CO) poisoning, meaning that the active sites may be contaminated with CO and not work any longer. For SOFC, slow startup time, compatibility issues between the electrolyte and electrodes, and the need of significant thermal shielding to retain heat are disadvantages. Therefore, there is a need to develop new types of fuel cells that circumvent these disadvantages and in this respect the so-called intermediate temperature (200-500 °C) fuel cell appears to be an attractive technology. However, due to the difficulty of developing electrolytes with sufficiently good properties, the development of intermediate temperature fuel cells has shown to be very difficult.

The primary challenge has been to develop electrolytes displaying sufficiently high ionic conductivities. Targeted values are above 0.1 S/cm and in this respect there is a lack of materials in the intermediate temperature range. This can be seen in Fig 1.1, which shows the proton and oxide-ion conductivities of the state of the art materials over a large temperature range. As seen here, the low temperature (<100 °C) proton conductors are polymer based, such as Nafion, which shows a high conductivity, but starts to dehydrate already at around 100 °C [1] as the proton conductivity of Nafion relies on the presence of water molecules. $CsHSO_4$ shows high proton conductivity, above 140 °C, but melts at around 200 °C [1] as it decomposes.

It has been found that some hydrated perovskites show high proton conduction at the upper limit of the intermediate temperature range [2]. Also it has been found that hydrated alkali thio-hydroxogermanates show high proton conduction at the lower part of the intermediate temperature range (100-300 °C) [3,4]. F. Zhao et al. investigated $BaCe_{0.7}In_{0.2}Yb_{0.1}O_{3-\delta}$ as a proton conducting electrolyte for intermediate temperature solid oxide fuel cells [5]. X. Wu et al. found that 20 mol% Sb-doped SnP_2O_7 shows proton conductivity of above 0.1 S cm^{-1} at 300 °C under un-humidified conditions [6]. C. Sun et al. reported the NH_4PO_3-$(NH_4)_2SiP_4O_{13}$ composite shows high proton conductivity at 150-250 °C [7]. Y. Jiang et al. reported that the NH_4PO_3-SiO_2-P_2O_5 composite as a potential electrolyte for intermediate temperature fuel cells [8]. In addition, brownmillerite type oxides, which may be viewed as oxygen deficient perovskite type oxides show high proton conduction upon hydration [9-12].

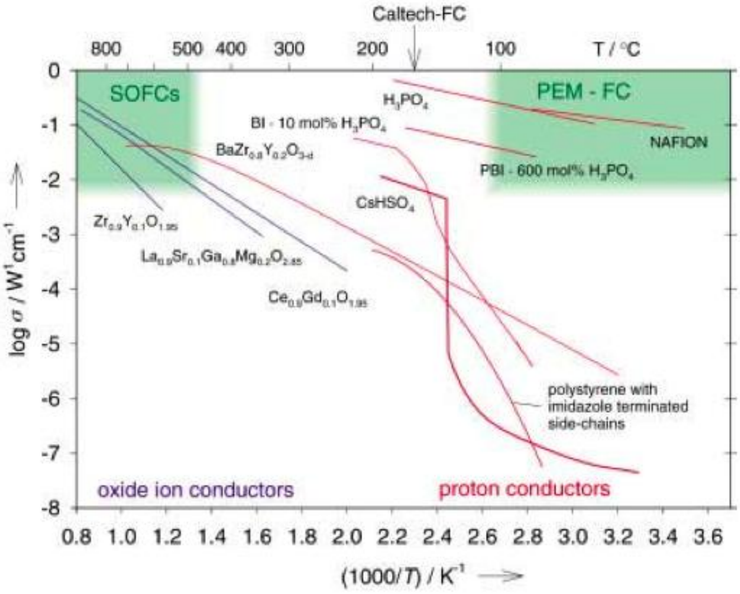

Figure 1.1: The conductivity of state of art materials. [Figure was taken from reference 13]

For the development of new materials, with proton conductivities beyond state of the art, it is crucial to increase the understanding of the basic science, such as structure and proton dynamics of those materials already known as well as to explore completely new compounds. In this regard, this Master thesis deals with investigations of local structure of the proton conducting brownmillerite type oxide system $Ba_2In_{1.85}M_{0.15}O_5$ (M=Ga, In, Y, Sc). These materials are reported to have an average-orthorhombic crystal structure, however, the local structure around the dopant atoms and protons (hydrated materials) may deviate from orthorhombic symmetry and is not yet known. The investigations have been performed using infrared spectroscopy techniques, well suited for local structural studies of materials.

CHAPTER 2

Proton conducting brownmillerite type oxides

Brownmillerite type oxides, of general chemical formula $A_2B_2O_5$, are oxygen deficient types of ABO_3 type perovskites[1] with ordered oxygen vacancies. Here, A represents a large cation, such as Ba^{+2}, Sr^{+2} and Ca^{+2}, while B represents small transition metal/main group cation, such as In^{+3}, Mn^{+3} and Al^{+3}. Examples of such materials are $Ca_2Mn_2O_5$, $Ca_2Al_2O_5$, $Sr_2Fe_2O_5$, $Ba_2Al_2O_3$, etc. Brownmillerites were initially proposed as oxide-ion conductors [1, 14], but later it was found that they can also be proton conducting, once prehydrated or under humid conditions [9,15].

$Ba_2In_2O_5$ is the most studied brownmillerite oxide for the studies on oxide ion conduction as well as proton conduction [9, 12, 14, 16-19].The reason for that is at 1000 °C $Ba_2In_2O_5$ has a conductivity comparable to that of yttria-stabilized zirconia, which is the most widely used solid state oxide-ion conductor. $Ba_2In_2O_5$ has an orthorhombic crystal structure from room temperature up to 900 °C with Icmm space group [20]. At 900 °C, the oxygen vacancies begin to disorder and at 925 °C, the crystal structure changes from orthorhombic to tetragonal structure. And finally at 1040 °C, $Ba_2In_2O_5$ becomes a cubic oxygen deficient perovskite [19]. The presence of intrinsic oxygen vacancies in the $Ba_2In_2O_5$ structure supports for a significant proton conduction. In $Ba_2In_2O_5$ intrinsic oxygen vacancies are ordered in a way that the room temperature structure contains alternating InO_6 octahedra and InO_4 tetrahedra. Because of this vacancy ordering it has low oxide ion conductivity at low temperatures. But, at 930 °C, there is a phase transition from orthorhombic to tetragonal symmetry, with a concomitant disordering of the oxygen vacancies. This vacancy disordering result in increasing the oxide ion conductivity by more than one order of magnitude [16, 21]. It has been found that the high-conductivity phase can be stabilized to lower temperatures by doping the material [22]. For example it has been reported that partial substitution of Ga^{+3} for In^{+3} decreases the phase transition temperature [23]. In addition to the high oxide-ion conductivity, proton conductivity has also been reported in such systems in wet atmospheres due to the incorporation of water [9, 24].

---

[1] The basic chemical formula of perovskites is ABO_3, where A represents a large divalent cation, such as Ba^{+2} or Sr^{+2} whereas B represents a small tetravalent anion such as Zr^{+4} or Ce^{+4}. The structure of the perovskite oxide (ABO_3) is simple cubic with space group Pm $\bar{3}$m.

In addition to the work on proton conductivity of pure $Ba_2In_2O_5$, investigations have been done for doped compounds, such as $Ba_2(In_{1-x}Ti_x)_2O_{5+x}$, $(Ba_{1-x}La_x)_2In_2O_{5+x}$, $Ba_2In_{1.8}Si_{0.2}O_{5.1}$ and $Ba_2In_{2-x}P_xO_{5+x}$ [25-28]. Kakinuma et al. [25] reported on conductivity measurements of $(Ba_{1-x}La_x)_2In_2O_{5+x}$ and found a maximum proton conductivity of 1.12×10^{-5} S cm^{-1} for x=0.10 at 400 °C. Quarez et al. [26] reported on conductivity measurements of $Ba_2(In_{1-x}Ti_x)_2O_{5+x}$ (x=0.2, 0.3 and 0.4) phases in dry and wet N_2 and found a maximum proton conductivity of 1.1×10^{-3} S cm^{-1} for x=0.2 at 450 °C for low levels of hydration. Noirault et al. [15] reported on the proton conductivity of $Ba_2(In_{0.65}Sc_{0.35})_2O_{4.2}\square_{0.2}(OH)_{1.6}$ [5.4×10^{-3} S cm^{-1} at 350 °C] and $Ba_2(In_{0.7}Y_{0.3})_2O_{4.35}\square_{0.35}(OH)_{1.3}$ [2.0×10^{-3} S cm^{-1} at 350 °C], whilst Shin et al. [27] found a conductivity of 2.4×10^{-3} S cm^{-1} at 400 °C in wet N_2 for $Ba_2In_{1.8}Si_{0.2}O_{5.1}$. J. F. Shin et al. reported the successful incorporation of phosphate and sulfate groups in $Ba_2In_2O_5$ and the results shown that incorporation of these oxi-anions leads to a structural conversion from an orthorhombic brownmillerite type to a disordered perovskite-type and hence increases the conductivity at temperature <800 °C [28].

2.1 The brownmillerite structure and incorporation of protons

The structure of the brownmillerite type oxides may be viewed as a perovskite-type structure in which one sixth of the oxide ions in the ideal perovskite parent structure are replaced by oxygen vacancies which are ordered along [101] directions in alternate (010) planes. This ordering gives the orthorhombic structure for brownmillerites with alternating layers of BO_6 octahedra and BO_4 tetrahedra, centered around the B atoms (Figure 2.1). As shown in this figure, there are three different types of oxygen sites. O(1) and O(3) are equatorial atoms in BO_6 octahedra and BO_4 tetrahedra respectively. O(2) atoms are apical oxygens, i.e. the oxygens belong to both tetrahedra and octahedra or in other words the oxygens which join the corners of tetrahedra and octahedra. The lattice parameter of Brownmillerite structure relates to the cubic lattice parameter (a_P) of the ideal perovskite as $a=\sqrt{2}a_P$, $b=4a_P$ and $c=\sqrt{2}a_P$.

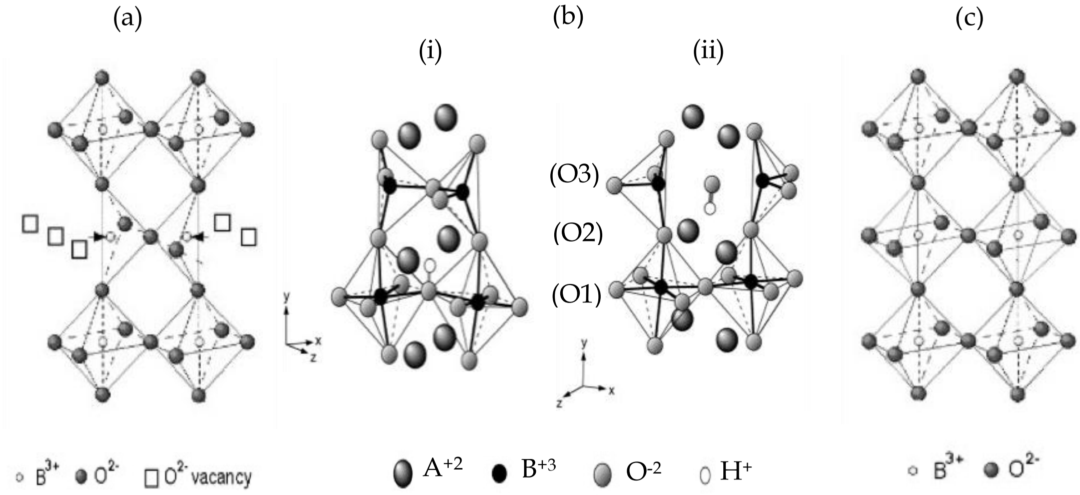
(a)
(b)
(c)
(i)
(ii)
(O3)
(O2)
(O1)
y
x
z
B^{3+} ● O^{2-} □ O^{2-} vacancy
A^{+2} B^{+3} O^{-2} H^{+}
B^{3+} ● O^{2-}

Figure 2.1: Schematic illustration of ideal (a) brownmillerites structure $A_2B_2O_5$ in dry phase (b) brownmillerites structure in hydrated phase (i) orientation of O-H pair occupying O(1) vacancy (ii) orientation of O-H pair at interstitial site (c) ideal perovskite structure ABO_3 (A cations have removed for clarity in (a) and (c)) [Figures were taken from references 11 and 29].

Protons can be incorporated in the brownmillerite structure by hydration. In a humid atmosphere, water molecules from the atmosphere are incorporated into the oxygen-deficient structure through the following reaction and the oxygen vacancies intrinsic of the brownmillerite structure get filled [12].

$$H_2O + V_O^{\cdot\cdot} + O_O^x \leftrightarrow 2OH_O^{\cdot}$$

Here $V_O^{\cdot\cdot}$ is an oxygen vacancy, O_O^x is the oxide ion, and $OH_O^{\cdot}$ is the hydroxyl ion, in the Kröger-Vink notation [30].

2.2 Proton conductivity of brownmillerites

The crystal structure of the hydrated phase can be described as a layered perovskite structure with alternating layers of oxygen octahedra (Fig. 2.1 (b)). The H(1) protons are covalently bonded to the O(2) oxygens while, forming hydrogen bond with one of the O(1) oxygens [31]. H(2) protons form both covalent and hydrogen bonds with O(3) oxygens [31].

The defect chemistry of the brownmillerite structure in $Ba_2In_2O_5$ favors both oxide-ion conduction as well as proton conduction [9]. Zhang et al. [9] reported that $Ba_2In_2O_5$ exhibits proton conduction at temperatures lower than 500 °C when the conductivity is measured in moist air and Schober et al. [24] confirmed proton solubility in $Ba_2In_2O_5$ in moist air at temperatures below 300 °C. It has been confirmed by several groups that the proton conduction of $Ba_2In_2O_5$ occurs in the crystal phase of $Ba_2In_2O_4(OH)_2$. In wet gas $Ba_2In_2O_5$ transforms to a layered perovskite structure ($a = b \approx ap$, $c \approx 2ap$) absorbing 1 mole of H_2O, a process that has been studied with for example in-situ PXRD [20]. Furthermore, Jankovic et al. [18] reported that $Ba_2In_2O_5$ can be proton conducting also in H_2 containing atmospheres rather than under wet conditions.

CHAPTER 3

Infrared spectroscopy

The main experimental technique used in this thesis work is infrared spectroscopy, which is a powerful technique to study the vibrational dynamics and local structure of materials. Infrared spectra are characterized by a number of vibrational (or absorption) bands (peaks), which are defined by their positions, strengths (intensities), and shapes, and represent a fingerprint of the local structural details of the material(s) under investigations. More specifically, the vibrational bands are associated with the vibrational modes of phonons and/or localized vibrational modes in the structure of the material(s), and by analyzing these one may obtain information about the local coordination of the vibrating species and in particular the local structural coordination around them.

3.1 The measurement principle

In an infrared spectroscopy measurement, the sample is irradiated by polychromatic light. When the frequency of the light matches the vibrational frequency of a bond, absorption may occur. Infrared light interacts with those vibrations whose dipole moment (μ) periodically changes due to the oscillation of the atoms. If the oscillating electromagnetic field of the incident photon couples with the dipole oscillating at the same frequency, it is absorbed. Figure 3.1 illustrates the principle of infrared absorption.

Frequencies of fundamental vibrations typically fall into a range of 10-4000 cm^{-1}, which is in the infrared region (10-14000 cm^{-1}) of the electromagnetic spectrum. In an infrared spectrum, most of the bands are related to fundamental vibrations, i.e. excitations from the vibrational ground state to the first excited state. The probability of occurring transitions from ground state to overtones is low.

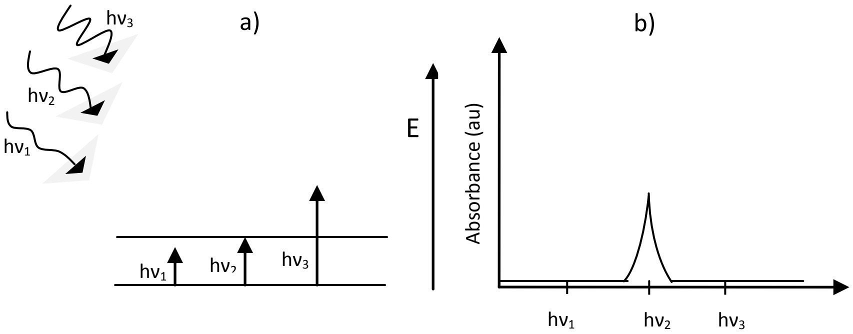

Figure 3.1: Illustration of the principle of infrared absorption: a) Photons with energies hν$_1$, hν$_2$ and hν$_3$ hit on a two level system. But only the photon with hν$_2$ energy is absorbed as only this photon has the same energy as the energy difference between the two vibrational states. b) The corresponding infrared absorption spectrum. [Figure redrawn from reference 32]

3.2 Measurements

The infrared spectroscopy measurements were performed in the range 40-4000 cm^{-1} using three different experimental setups. The experiments in the range 40-1000 cm^{-1} were performed in transmittance mode using a Bruker IFS 66v/s FT-IR spectrometer equipped with a DTGS detector and exchangeable beam splitters; Mylar 6 (40-400 cm^{-1}) and KBr (400-1000 cm^{-1}). An extensive sample preparation was needed for the measurements in the frequency range 40-1000 cm^{-1}. In transmittance mode, the sample should be neither too absorbing nor too transparent. In my case, the samples were dispersed to typically 6 wt% in 0.1 g polyethylene for the far-IR part (40-400 cm^{-1}) and 6 wt% in 0.1 g KBr for mid-IR part (400-1000 cm^{-1}) and pressed into pellets. In order to obtain the final Ø13 mm pellets, a load of 7 ton was applied to the powder mixtures. The reference spectra were obtained from measurements on pure polyethylene and KBr pellets with the same dimensions as the sample pellets. The absorbance spectrum was derived by taking the ratio between the reference spectrum and the sample spectrum.

The experiments in the range 1750-4000 cm^{-1} was performed in diffuse reflectance mode using a Bruker Alpha FT-IR spectrometer with ALPHA-R module equipped with a KBr beam splitter and a DTGS detector. Experiments in this region were done inside a glove box.

3.3 Instrumentation

3.3.1 Bruker Alpha FT-IR spectrometer (ALPHA-R module)

The ALPHA-R module is designed for measurements in diffuse reflection. The optics of this module is designed in such a way that to detect optimized diffusely reflected light and to detect minimized specularly reflected light.[1] DRIFTS (Diffuse Reflectance Infrared Fourier Transform Spectroscopy) is the analyzing technique use in this module. This DRIFT module allows to analyze various kind of solid samples such as powders, inorganic materials, gem stones, papers, textiles and others. Easy sampling handling and high light throughput are advantages of the DRIFT module.

3.3.2 Bruker IFS 66 v/s FT-IR spectrometer

Figure 3.2 shows a schematic picture of a Bruker IFS 66 v/s FT-IR spectrometer. The main three parts of the spectrometer are the polychromatic light source, the Michelson interferometer and the detector. In this thesis work, a SiC rod was used as the source. The Michelson interferometer consists of two mirrors, one fixed and the other moving, and a beam splitter. The Bruker IFS 66 v/s spectrometer can be used with different types of insertion devices in the sample chamber, which allows for different measuring modes. But, it is important to choose the proper beam splitter and the detector. For example, in this thesis work a Mylor 6 beam splitter and a DTGS detector was used for the measurements in the far-IR region while a KBr beam splitter and a DTGS detector was used for the measurements in the mid-IR region. As shown in the figure, one half of the intensity of the incident light passes through the beam splitter and reflects back on the moving mirror while the other half reflects on the beam splitter and reflects back on the fixed mirror. Two reflected beams recombine into an interferogram, which is then directed towards the sample chamber and to the sample. The sample absorbs particular wavelength of the incoming light depending on its microscopic structure and composition. The detector registers the intensity of the light passes through the sample. A DTGS detector was used in this work. The detected light is finally Fourier transformed to obtain the sample spectrum.

[1] Reflected light consists of the two components, diffusely and specularly reflected light. Specular component is the radiation that is reflected directly from the sample surface whereas the diffuse part is the radiation that undergoes multiple scattering and emerges in various directions. In diffuse reflectance spectroscopy, the specular part is blocked and only the diffusely reflected light is collected and directed towards the detector and vice versa.

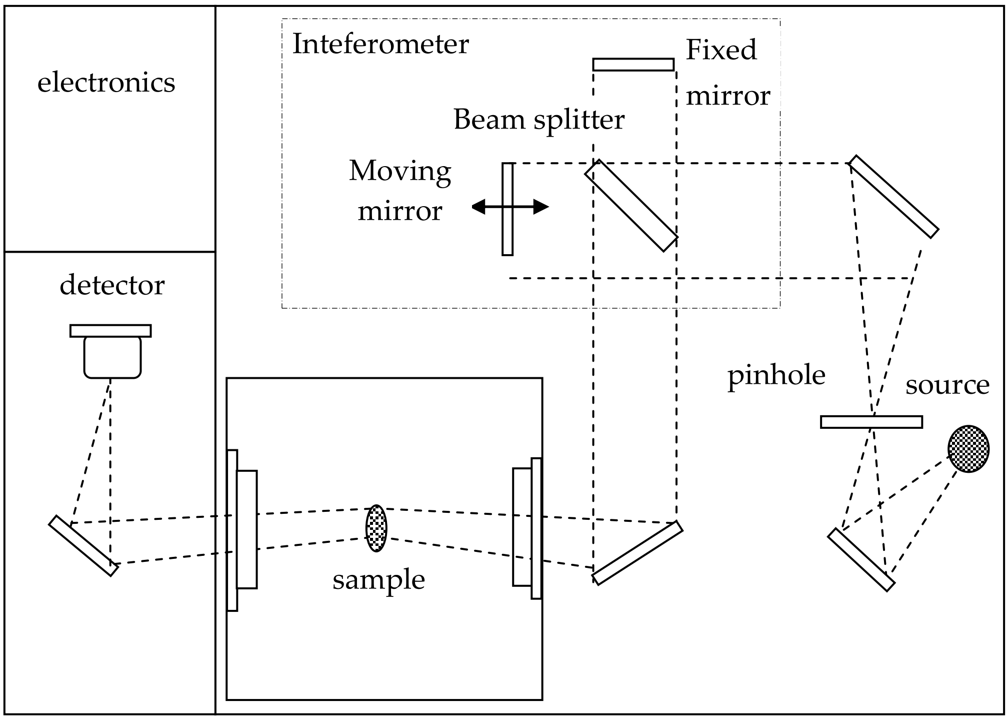
electronics
Inteferometer
Fixed
mirror
Beam splitter
Moving
mirror
detector
pinhole
source
sample

Figure 3.2 Schematic diagram of the Bruker IFS 66 v/s FTIR spectrometer. [The figure is redrawn from reference 32].

CHAPTER 4

Results and discussion

This chapter describes all the results which I got from my infrared experiments followed by a discussion. The results are described in two parts, according to the measured frequency ranges (40-1000 cm^{-1} and 1750-4000 cm^{-1}).

4.1 Results in the frequency range 40 – 1000 cm^{-1}

Figure 4.1 shows the IR spectra of dry and hydrated samples of $Ba_2In_{1.85}M_{0.15}O_5$ (M = In, Sc, Ga and Y) in the range of 40 – 1000 cm^{-1}.

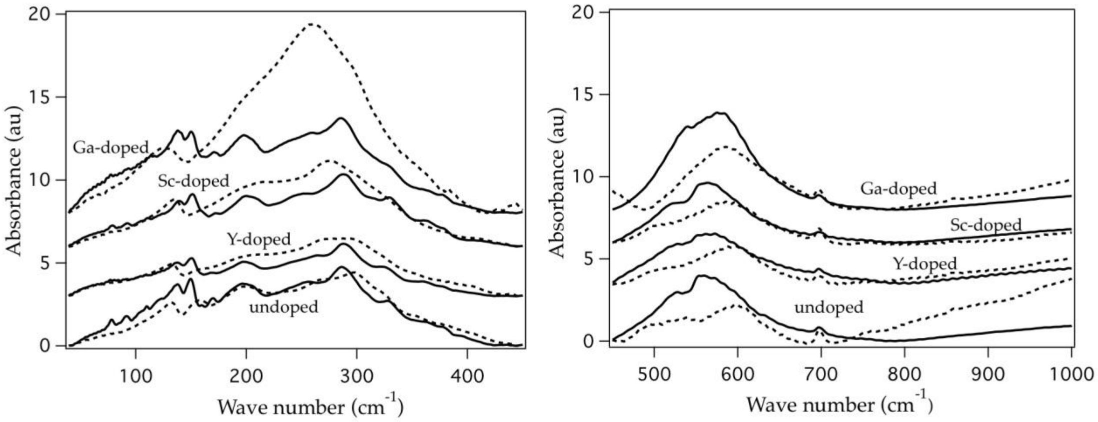

Figure 4.1: IR spectra of dry and hydrated samples in the frequency range of 40 – 1000 cm^{-1}. Solid lines represent dry materials and dashed lines represent hydrated materials.

First consider the spectra of the dry (dehydrated) samples. If we take a look on the spectra of the undoped sample we can see strong bands at 140 cm^{-1}, 150 cm^{-1}, 200 cm^{-1}, 290 cm^{-1}, 330 cm^{-1} and 560 cm^{-1} with weak bands at below 100 cm^{-1} and at 700 cm^{-1}. The peaks can be assigned as In-O bending modes at around 330 cm^{-1} and In-O stretching modes at 560 cm^{-1} [33, 34]. Bands below 140 cm^{-1} should arise from Ba vibrations whereas the band at 700 cm^{-1} should occur from impurities [34]. We can observe that some bands have slightly shifted towards higher frequencies for the doped samples. The frequency shift is higher for the Sc doped materials than for the Ga and Y doped equivalents and relates to a change of the bond strength(s) of the vibrating unit(s). A strong bond results in a high vibrational frequency, and vise-versa. Therefore, the results indicate that the bond strengths related to some oxygen modes increase with the introduction of dopant atoms upon doping with the trivalent ions.

When considering the spectra for hydrated samples, we can see a reduction in the number of bands. It is clear that the spectrum of the undoped sample is different from the doped ones, which are similar in shape. The undoped sample shows five peaks at around 130 cm^{-1}, 160 cm^{-1}, 200 cm^{-1}, 275 cm^{-1} and 600 cm^{-1}, respectively. However, we cannot see the two bands at around 160 cm^{-1} and 200 cm^{-1} for the doped samples. Furthermore, the shifting of the positions of some bands with doping, and depending on the type of the dopant atom, is indicative of dopant-induced structural distortions.

4.2 Results in the frequency range 1750 – 4000 cm^{-1}

Figure 4.2 shows the IR spectra of dry and hydrated $Ba_2M_2O_5$ samples in the frequency region of 1750 – 4000 cm^{-1}.

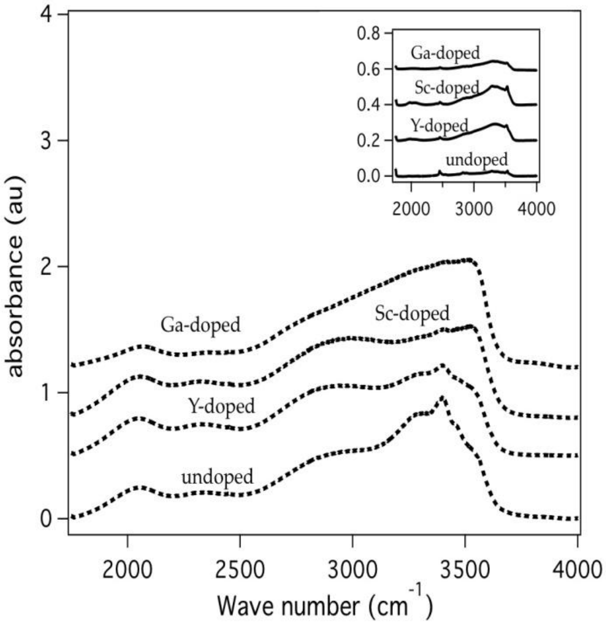

Figure 4.2: IR spectra of hydrated samples in the frequency range of 1750 – 4000 cm^{-1}.Inset shows the IR spectra of dry samples in the same frequency region.

In the given region, compared to the undoped sample in the dry phase, doped samples have different spectra. Among them, the spectra for the Y and Sc doped ones are quite the same. We can see two peaks at around 2050 cm^{-1} and 2350 cm^{-1} with a broad peak between 2600 – 3600 cm^{-1}, which corresponds to the O-H stretch vibration. For the dry samples, we also observe an O-H stretch band, although much weaker than for the hydrated materials. Although the dehydrated materials have been vacuum dried at 800˚C, it was obviously not possible to remove all the water from the materials and the reason for that is not really understood.

When considering the spectra for the hydrated samples, we can see a clear intensity increment in the O-H stretch bands. The large intensity increment of the O-H stretch band upon hydration confirms the incorporation of O-H species into the material structure. Although the spectra for the doped samples differ from the undoped one, they all show some common features. We can see the two peaks below 2500 cm^{-1} that are visible in dry samples, remains in hydrated ones also with intensity increment. We can see a broad intense peak between 2600-3600 cm^{-1}.

It can be suggested that the two bands at around 2050 cm^{-1} and 2350 cm^{-1} are related to the O-H stretch vibrations with the protons located in environments which locally deviate from the average structure [35]. The broad nature of the O-H band is related to the distribution of hydrogen bond strengths between the proton and neighboring oxygen. In other words, because of the different local environments for the protons, the O-H stretch band has broadened.

In order to carry out a more detailed analysis of the spectral features, I performed a peak fit analysis. The peak fit analysis was performed using six Gaussian bands (A-F) and a linear baseline for the frequency range 1750-4000 cm^{-1}. Among the six Gaussian bands, two were used for the bands at 2050 and 2350 cm^{-1} while the broad band in the region 2600-3600 cm^{-1} was reproduced by four bands. The sum of the Gaussian bands fits well with the experimental spectra. As an example, Figure 4.3 shows the peak fittings for the undoped (hydrated) sample.

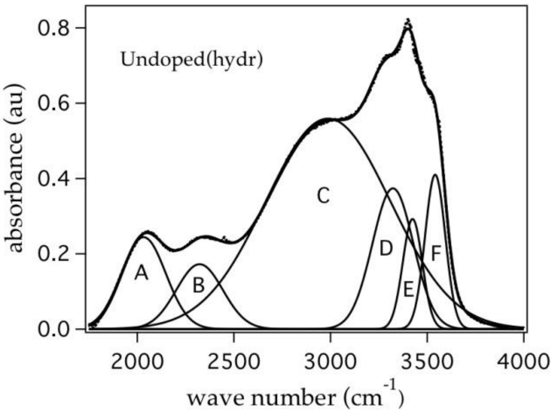

Figure 4.3: Peak fit for the hydrated $Ba_2In_2O_5$ sample with six Gaussian bands.

The six Gaussians may be assigned according to the strength of the hydrogen bonding between the proton and a neighboring oxygen. In this context, it may be suggested that the two lowest frequency bands at 2050 cm^{-1} and 2350 cm^{-1} (A and B) are likely to correspond to sites with (very) strong H-bonding, the bands C and D should then correspond to sites with middle H-bonding, whereas bands E and F then corresponds to sites with weak H-bonding. Also it may be suggested that the protons in locally symmetric environments, such as In-OH-In and Sc-OH-Sc results in quite narrow bands whereas, the protons in locally mixed/non-symmetric environments, such as In-OH-Ga, In-OH-Sc and/or close to an oxygen vacancy may result in broader bands. Hence, the bands C and D may be associated to protons in mixed environments and/or close to oxygen vacancies, while bands E and F may be associated to protons in locally symmetric environments. Furthermore, it can be suggested that the quite broad C band can be decomposed into several sub-bands which are associated to several O-H stretch modes result from various nonsymmetrical configurations of protons.

Figure 4.4 (a) shows how the positions of those bands change with the type of the dopant while figure 4.4 (b) shows how the relative integrated intensities change for the six Gaussian bands for hydrated samples.

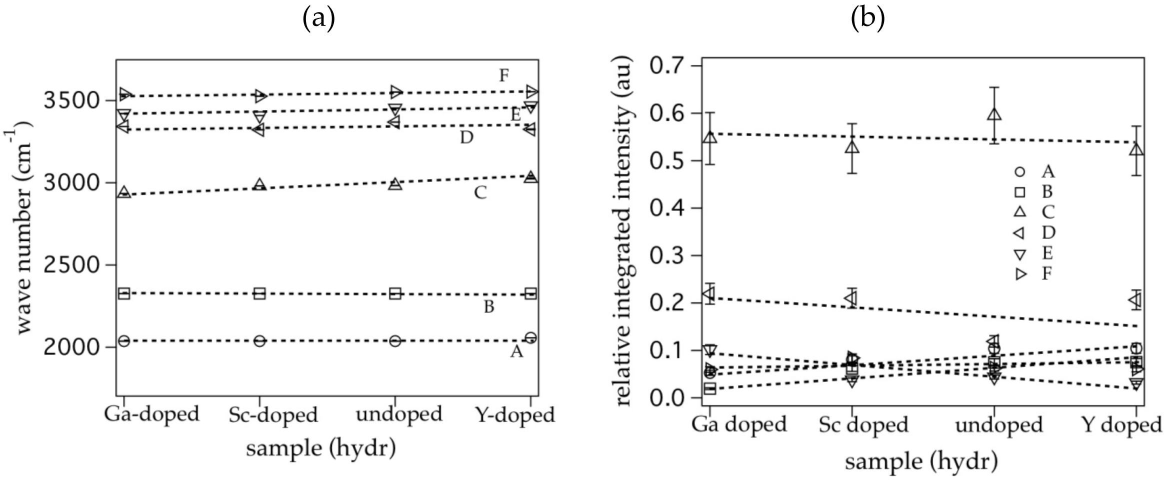

Figure 4.4: (a) Positions (b) Relative integrated intensities of the six Gaussian bands for the hydrated samples. Dashed lines serve as guide to the eye.

The result of this analysis indicates that the positions of the bands A and B are independent of the type of dopant ion. The bands C-F have shifted slightly to lower frequency for the Ga and Sc doped samples, while they have shifted a little bit to higher frequency for the Y doped one. That is, it appears that the smaller the radius of the dopant, the higher the tendency for stronger hydrogen bonding (the atomic radii of the dopant varies according to Ga<Sc<In<Y). Furthermore,

according to the analysis of the peak positions of the Gaussian bands, it can be seen that band C has red-shifted more than bands D-F for the Ga and Sc doped samples. This indicates that protons associated to band C are more affected by the doping than those associated with bands D-F.

According to figure 4.4 (b), we can also see that bands C and D show the highest relative intensity. With increasing atomic radius of the dopant, the relative intensity of bands C, D and E decreases and that of bands A, B and F increases. Since the intensity of the O-H stretch band is related to the number of protons in the material, it is clear that the proton concentration is high in environments with middle (intermediate) H-bonding and this amount decreases with the increasing atomic radius of the dopant. It follows that the doping with a larger ion results in a redistribution of protons from middle hydrogen bonding sites to sites where the degree of hydrogen bonding is stronger and weaker.

CHAPTER 5

Conclusions

A spectroscopic study has done on the hydrated brownmillerite $Ba_2In_{1.85}M_{0.15}O_{5-\delta}$ (M = In, Ga, Sc and Y) using infrared spectroscopy to investigate how the local structure and in particular local proton configurations depend on the type of dopant atom.

From the spectroscopical analysis, it was possible to see the structural distortions with the incorporation of dopants to the $Ba_2In_2O_5$ compound. It was possible to see that hydrogen bonding formation is higher for the dopants with smaller atomic radius. Also it was possible to see that the proton concentration is highest in environments with intermediate hydrogen bonding and that some of these protons redistribute to sites with either stronger or weaker hydrogen bonding as the radius of the dopant atom is increased.

Appendix A

Fuel cells

A.1 Basics of fuel cells

Fuel cells are electrochemical devices, which convert chemical energy into electrical energy in an environmental friendly way. Inside a fuel cell, oxygen and hydrogen rich fuel combine to form water. So the fuel is not combusted like in internal combustion engines.

Every fuel cell has three main components; a positive electrode called cathode, a negative electrode called anode and an electrolyte, which carries ions from one electrode to the other. Among these three parts, the electrolyte plays the key role. Besides the above-mentioned three parts, a catalyst, such as platinum is often used to speed up the reaction at the electrodes.

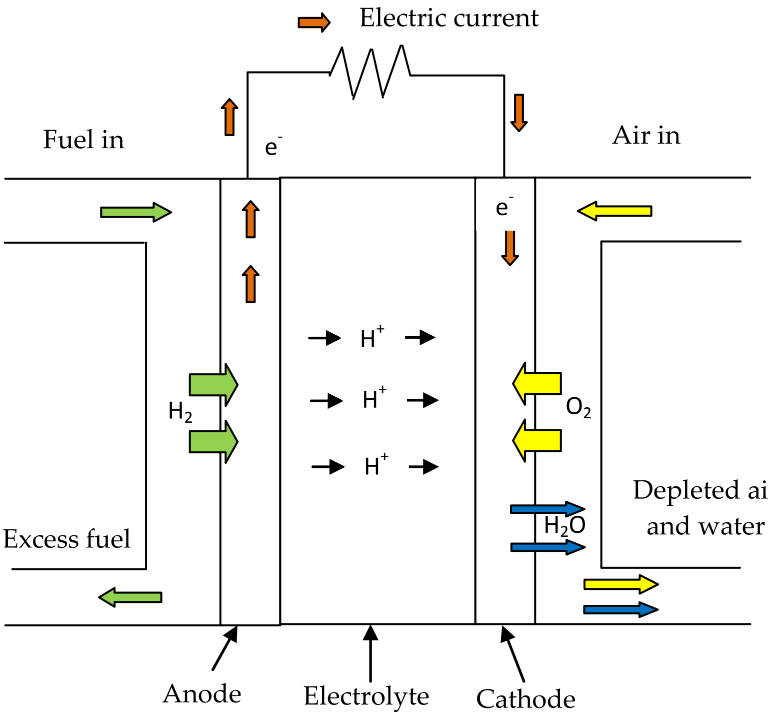
Electric current
Fuel in
e^-
Air in
e^-
H^+
H^+
H^+
H_2
O_2
Depleted air and water
H_2O
Excess fuel
Anode
Electrolyte
Cathode

Figure A.1: A schematic diagram of a solid oxide fuel cell (SOFC) utilizing proton conducting electrolyte.

A.2 Types of Fuel cells

There are several types of fuel cells, which are classified according to the nature of the electrolyte.

This thesis is focused on materials which are of interest for use as electrolytes in next-generation solid oxide fuel cells, which function by hydrogen and oxygen. However several other types of fuel cells exist. Examples of the most important are:

Proton exchange membrane fuel cell (PEMFC)

The proton exchange membrane fuel cell (PEMFC) uses a water-based, acidic polymer membrane as electrolyte and platinum-based electrodes. As PEMFCs operate at relatively low temperatures (<100 °C), use of pure hydrogen is a must. PEMFC are currently the leading technology for light duty vehicles and materials handling vehicles.

Direct methanol fuel cell (DMFC)

The direct methanol fuel cell (DMFC) also uses polymer membrane as an electrolyte like in PEMFC. The platinum-ruthenium catalyst on the DMFC anode draws the hydrogen from liquid methanol by eliminating the need for a fuel reformer. Therefore pure methanol can be used which is cheap but has a high energy density and can be easily transported and stored. DMFCs operate in the temperature range of 60 – 130 °C and used in applications such as mobile electronic devices or chargers and portable power packs.

Solid oxide fuel cell (SOFC)

The electrochemical process of a solid oxide fuel cell (SOFC) is based on the chemical reaction between hydrogen (at the anode) and oxygen (at the cathode) to produce water. The electrolyte serves as a barrier to gas diffusion but allows ion transport (either oxide or protons). Figure A.1 represents a schematic diagram of a SOFC utilizing proton conducting electrolyte. SOFCs work at very high temperatures (800 – 1000 °C) while having 60% - 80% efficiency. Because of the high operating temperature no need an external reforming or a metal catalyst. However, longer start up time, use of robust and heat-resistant materials for constructions are some of the disadvantages. SOFCs have three different geometries named planar, coplanar and micro-tubular. Because of the high efficiency, low emissions and fuel flexibility, SOFCs are of high interest. SOFCs are widely used in large and small stationary power generation. Improving

SOFC technology in a way to reduce the working temperature to 500-700 °C is an important challenge.

Alkaline fuel cell (AFC)

The alkaline fuel cell (AFC) uses an alkaline such as potassium hydroxide in water as its electrolyte while using pure hydrogen and oxygen as fuel. The typical operating temperature of AFCs is around 70 °C. Because of the low temperature, non-precious metals can be used instead of platinum. Nickel is the most commonly used catalyst in AFCs.

Molten carbonate fuel cell (MCFC)

The molten carbonate fuel cell (MCFC) uses a molten carbonate salt in a porous ceramic matrix as its electrolyte. The operating temperature of MCFC is around 650 °C. MCFCs operate with different fuels such as coal-derived fuel gas, methane or natural gas. MCFCs are used in large stationary power generations.

Phosphoric acid fuel cell (PAFC)

The phosphoric acid fuel cell (PAFC) uses phosphoric acid as its electrolyte and its electrodes are made of a finely dispersed platinum catalyst on carbon and a silicon carbide structure. PAFCs operate at moderately high temperatures of around 180 °C. PAFCs are used in stationary power generators with 100 – 400 kW power output.

Acknowledgements

Foremost, I would like to express my sincere gratitude to my supervisor Assistant professor Maths Karlsson for his support and guidance in the time of research and writing of this thesis.

My special thanks go to Mr. Habibur Rahman, who synthesized all the samples for me.

My sincere gratitude to Dr. Christopher Knee for sharing ideas with us by having valuable discussions.

Then, I would like to thank Dr. Ezio Zhanghellini for his support on instrument handling.

Also, I would like to thank all the members in KMF group for their support and sharing the facilities with me.

The support and encouragements from my parents and all family members are gratefully acknowledged.

I would like to thank all my Sri Lankan friends, who live in göteborg for their encouragements to succeed my studies here.

Last, but not least I would like to thank my husband Jagath for his never ending support, guidance and encouragements. At the same time, my loving thanks to my two daughters Sayuni and Dasuni for their support.

Bibliography

1. T. Norby, Solid State Ionics 125, 1 (1999).
2. K. D. Kreuer, Ann. Rev. Mater. Res. 33, 333 (2003).
3. S. A. Poling, C. R. Nelson, S. W. Martin, Chem. Mater. 17, 1728 (2005).
4. S. A. Poling, C. R. Nelson, S. W. Martin, Materials letters 60, 23 (2006).
5. F. Zhao, S. Wang, L. Dikson, F. Chen, J. Power Sources 196, 7500 (2011).
6. X. Wu, A. Verma, K. Scott, Fuel cells 8, 453 (2008).
7. C. W. Sun, U. Stimming, Electrochim.Acta 53, 6417 (2008).
8. Y. Jiang, T. Matthieu, R. Lan, X. Xu, P. I. Cowin, S. Tao, Solid state Ionics 192, 108 (2011).
9. G. B. Zhang, D. M. Smyth, Solid State Ionics 82, 153 (1995).
10. T. Schober, Solid State Ionics 109, 1 (1998).
11. C. A. J. Fisher, M. S. Islam, Solid State Ionics 118, 355 (1999).
12. W. Fisher, G. Reck, T. Schober, Solid State Ionics 116, 211 (1999).
13. K. D. Kreuer, ChemPhysChem 3, 771 (2002).
14. A. Rolle, R. N. Vannier, N. V. Giridharan, F. Abraham, Solid State Ionics 176, 2095 (2005).
15. S. Noirault, E. Quarez, Y. Piffard, O. Joubert, Solid State Ionics 180, 1157 (2009).
16. J. B. Goodenough, J. E. Ruiz-Diaz, and Y. S. Zhen, Solid State Ionics 44, 21 (1990).
17. S. B. Adler, J. A. Reimer, J. Baltisberge,r and U. Werner, J. Am. Chem. Soc. 116, 675 (1994).
18. J. Jankovic, D. P. Wilkinson, and R. Hui, J. Electro. Soc. 158, B61 (2011).
19. A. Mancini, J. F. Shin, A. Orera, P. R. Slater, C. Tealdi, Y. Ren, K. L. Page, and L. Malavasi, Dalton Trans. 41, 50 (2012).
20. P. Berastegui, S. Hull, F. J. García-García, and S.-G. Eriksson, J. Solid State Chem. 164, 119 (2002).
21. S. A. Speakman, J. W. Richardson, B. J. Mitchell, S. T. Misture, Solid State Ionics 149, 247 (2002).
22. C.A.J. Fisher et al,in oxygen ion conductors and their technological applications 1996,56,25.
23. M. Yoshinaga, M. Yamaguchi, T. Furuya, S. Wang, T. Hashimoto, Solid State Ionics 169, 9 (2004).
24. T. Schober, J. Friedrich, F. Krug, Solid State Ionics 99, 9 (1997).
25. K. Kakinuma, A. Tomita, H. Yamamura, T. atake, J. Mater. Sci. 41, 6435 (2006).
26. E. Quarez, S. Noirault, M. T. Caldes, O. Joubert, J. Power Sources 195, 1136 (2010).
27. J. F. Shin, D. C. Apperley, and P. R. Slater, Chem. Mater. 22, 5945 (2010).
28. J. F. Shin, A. Orera, D. C. Apperley, and P. R. Slater, J. Mater. Chem. 21, 874 (2011).
29. S. F. Matar, J. Etourmeau, Int. J. Inorg. Mater. 2, 523 (2000).
30. F. A. Kröger, H. J. Vink, SolidState Physics: Advances in Research and Applications, Academic Press, 1956.

31. Structure and Dynamics in Transition Metal Perovskites, Doctoral Thesis of Johan Bielecki, 2012.
32. Solid state proton conductors, Doctoral thesis of Maths Karlsson, 2007.
33. M. Karlsson, A. Matic, C. S. Knee, I. Ahmed, S. Eriksson, and L. Börjesson,Chem. Mater. 20, 3480 (2008).
34. C. Tennailleau, A. Pring, S. M. Moussa, Y. Liu, R. L. Withers, S. Tarantino, M. Zhang, M. A. Carpenter, J. Solid State Chemistry 178, 882 (2005).
35. M. Karlsson, A. Matic, E. Zanghellini, and I. Ahmed, J. Phys. Chem. C 114, 6177 (2010).